Tracking of cogging stiffness using the multi-bin SDFT

Foeke Vanbecelaere [a,b,*], Jasper De Viaene[a,b], Michael Monte[a,b], Kurt Stockman[a,b]

[a]*Department of Electromechanical, Systems and Metal Engineering, Ghent University, Belgium*
[b]*FlandersMake@UGent - Corelab MIRO*

Abstract

Due to the high power density and wide speed range, a permanent magnet synchronous motor (PMSM) is commonly used in industry. Efficient production requires optimized motion control of the mechanism driven by the PMSM. Unfortunately, designing the controller is usually based on a model of the mechanism without including parameters originating from the motor. Cogging stiffness originates from the magnetic forces between rotor magnets and stator teeth and is one of these forgotten parameters. The performance is sub-optimal when this stiffness is not considered during control design. The stiffness also changes over time due to changing load conditions such as temperature.

Aiming for optimized motion control of high-speed mechanisms, this paper proposes to expand the classic motion controller with an on-line stiffness tracker. The tracker is based on the sliding Discrete Fourier Transform (SDFT). The tracking technique is conceptually analysed and experimentally validated on a PMSM-driven rod. The classic Welch technique having an update time of at least 100 s is used as a benchmark. With similar accuracy and a much faster update time of 1.25 ms, the stiffness is tracked on-line using SDFT. The developed stiffness tracker is implemented on the provided commercial motion controller, proving its computational efficiency.

Keywords: Parameter tracking, System identification, Sliding discrete Fourier transform (SDFT), Harmonic extraction, Gauss-Newton algorithm, Permanent magnet synchronous motor (PMSM), Cogging torque

1. Introduction

Permanent magnet synchronous motors (PMSMs) are commonly used for driving single-actuated mechanisms because of their advantages such as high power-density ratio, wide speed range and fast dynamic response. A disadvantage leading to inaccuracy is a torque ripple caused by the attractive forces between the permanent magnets on the rotor and the steel slots on the stator. This ripple is known as the cogging torque (Keyhani et al., 1999). The magnets on the rotor are pulled towards the equilibrium positions where the magnetic forces cancel each other out.

Two approaches are found in the literature to tackle the cogging effect. The first one is improving the motor design. A few examples are magnet and slot skewing (Ocak and Aydin, 2020; Ueda et al., 2016; Shi et al., 2019; Mengesha et al., 2021), fractional slots (Dang et al.,

*Corresponding author, contact: foeke.vanbecelaere@ugent.be

2019; Nguyen et al., 2010; Zhao et al., 2018), teeth width variation (Petrov et al., 2015), pole-arc optimization (Jiang, 2023), magnet placement and shape optimization (Anuja and Doss, 2021; Islam et al., 2007), tooth tip optimization (Brescia et al., 2021), etc. All of these concepts are validated through finite element analysis, leading to promising cogging torque reductions (Gilardi et al., 2011). But when cost and complexity are considered many solutions are abandoned or the full potential is not realized.

The second approach is to improve the motion controller. In (Bu et al., 2021) a torque signal is added to the speed controller output resulting in smooth shifts of the equilibrium positions. Another technique is to expand the controller with a disturbance observer (Wu et al., 2020). Or in (Houari et al., 2018) a high-pass filter is added to the torque-generating current for suppressing the cogging harmonics. Among others, these techniques are validated on experimental setups and can easily be implemented in the industry as no additional hardware is required. The improvements are however sub-optimal because the change of the cogging torque over time due to e.g. temperature changes (Duan et al., 2021) is not considered.

As depicted in figure 1, this paper proposes to expand the classic motion controller with an on-line stiffness tracker. The stiffness represents the position derivative of the cogging torque. Based on the machine requirements, a cyclic motion profile is defined which relates the desired position θ^* of the mechanism with time t. A sensor, typically a built-in encoder on the motor shaft, measures the actual position θ. Based on the error between θ^* and θ, a control algorithm calculates the desired motor torque T^*_{m} with the objective to minimise this error.

Common practice is to add both a speed- and torque feedforward enabling faster and more accurate motion performance (Van Oosterwyck et al., 2019). The speed feedforward provides the desired speed Ω directly to the speed controller and the torque feedforward provides the desired torque T^*_{m} directly to the current controller. The purpose of the stiffness tracker is to maintain optimised motion control by using the tracked stiffness $\hat{k}$ and damping $\hat{b}$ as feedback for the motion profile definition, feedforward definition and controller tuning.

An important criterion shown in figure 1 is the parameter update time t_p. Due to the high-speed operation, it is desired to have fast updates. Next to that, the required memory of the stiffness tracker must be low to be implementable on the provided motion control platform. A computationally efficient technique is to use the sliding discrete Fourier transform (SDFT) for on-line parameter tracking. Both efficiency and accuracy are proven in (Vanbecelaere et al., 2020,

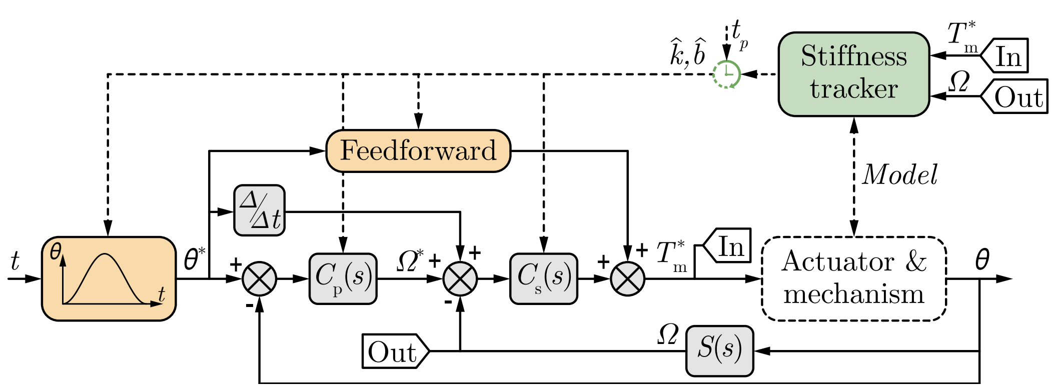

Figure 1: Classic control scheme for high-speed single-actuated mechanisms.

2022) where a single tracking frequency is injected, resulting in on-line estimates of the varying inertia of a PMSM-driven multi-body mechanism. In (Vanbecelaere et al., 2023) a multi-sine of 5 harmonics is injected, leading to simultaneous on-line estimates of mass, stiffness, and damping of a lumped mass-spring system. The tracking capability is however not investigated as the parameter values are constant. Experimental validation is also not included.

Building upon the previous works, the main research objective is to investigate the capabilities of using SDFT for tracking changing stiffness and damping. Accurately tracking the stiffness is the most important because this parameter determines the motion accuracy. The potential tracking errors are revealed and it is shown how to suppress them. The developed parameter tracker is evaluated in terms of update time and accuracy. The accuracy is compared with the commonly used off-line technique, namely the Welch technique (Saarakkala and Hinkkanen, 2015; Wahrburg et al., 2017).

After this introduction, section 2 presents the experimental setup and its model. The cogging effect is explained and how to linearize the cogging torque. The control scheme during parameter tracking is discussed. In section 3, the SDFT is implemented for parameter tracking. Tuning rules for achieving accurate results are presented. The maximum achievable accuracy is investigated through simulations. Section 4 presents the experimental results including a benchmark with the Welch technique. A conclusion is formulated in section 5.

2. Experimental setup

2.1. Motion equation

The experimental setup is shown in figure 2a and consists of a 6p18s PMSM of which the rotor is directly bolted to a rod. The PMSM has a nominal speed of 4000 min^{-1} and nominal torque of 1.11 N m. The CAD drawing is shown in figure 2b. From the CAD assembly, the inertia of the rod is found as $J_\mathrm{l} = 288\,\mathrm{kg\,mm^2}$. From the datasheet, the inertia of the rotor is given as $J_\mathrm{r} = 27\,\mathrm{kg\,mm^2}$.

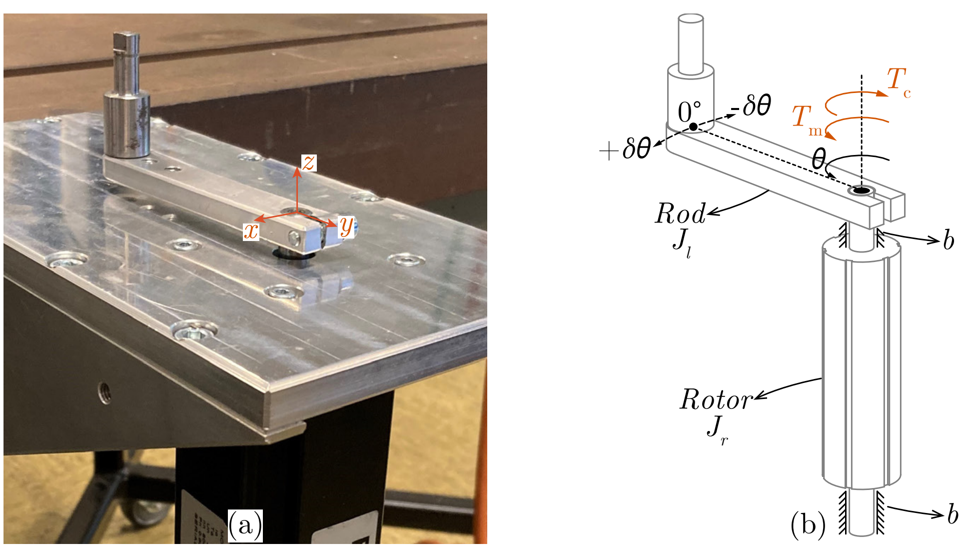

Figure 2: Experimental setup (a) and CAD drawing (b).

Both inertia values are defined around the z-axis which is aligned with the rotation axis of the rotor. The total inertia equals $J = J_r + J_l = 315\,\mathrm{kg\,mm^2}$. The torque on the z-axis originates from the motor torque T_m and cogging torque T_c. Due to the movement in the horizontal xy-plane, gravity does not contribute to the dynamics. The rotor is mounted on the frame with bearings of which the rotational friction is modelled as a viscous damper with damping value b.

Using Newton's second law with θ being the actuated position, $\Omega = \dot{\theta}$ being the speed and $\alpha = \ddot{\theta}$ being the acceleration, the motion equation is found:

$$\begin{aligned} \circlearrowleft\!+ \sum T_z &= J\alpha \\ T_m - T_c(\theta) &= J\alpha + b\Omega \end{aligned} \tag{1}$$

The setup in figure 2 is positioned at a stable equilibrium θ_{eq} where the deflection is defined as $\delta\theta = \theta - \theta_{eq} = 0°$ and where the cogging torque equals $T_c = 0\,\mathrm{N\,mm}$. As explained in the next subsection, the cogging torque T_c is position-dependent and has multiple stable equilibrium positions.

2.2. *The cogging effect*

In the case of a PMSM, cogging torque is produced by the magnetic attraction between the permanent magnets on the rotor and the stator teeth. This is clarified by a cross-section of a 2-pole/4-slot (2p4s) PMSM in figure 3. This type of PMSM does not exist in practice and only serves for clarification of the cogging effect. The rotor is equipped with a magnet having a north (N) and south (S) oriented pole. The stator, typically made of stacked laminated steel, has 4 slots and teeth. The slots are filled with copper windings.

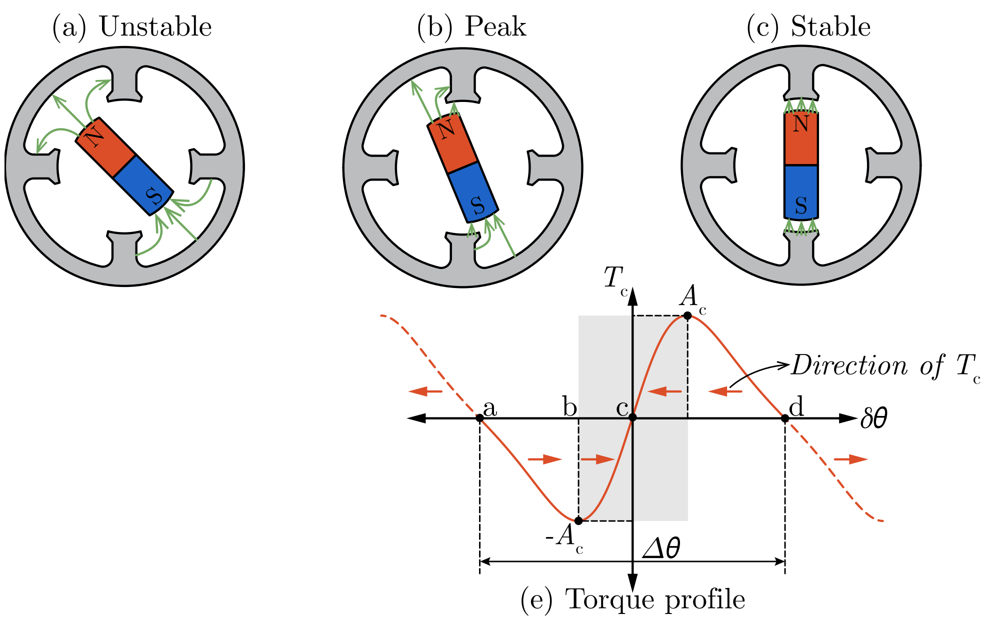

Figure 3: Cross section of a 2p4s PMSM with the indication of the flux lines in positions of an unstable equilibrium (a), a peak (b), a stable equilibrium (c) and a next unstable equilibrium (d) and the accompanying cogging torque profile (e).

In the figure, four positions of the rotor are shown with the magnetic flux lines in the air gap drawn in green. The preferred path of the flux is the one with the lowest magnetic reluctance. Because the permeability of steel is much higher than air, the flux prefers the shortest path through the stator teeth and lamination. This results in attractive forces that attempt to maintain the alignment between the teeth and magnets. This alignment is shown in position figure 3c. In position 'c', the different components of magnetic forces cancel out. Thus, no net cogging torque T_c is produced. A slight deflection of the rotor from 'c' results in cogging torque T_c which attempts to re-align the rotor to its stable equilibrium.

In figure 3e, a typical cogging torque cycle is depicted. The shape of the torque is inspired by simulations in (Wang et al., 2019; Yang and Wang, 2022) using finite element analysis. The peaks are noted with A_c. In position 'a', equilibrium is achieved because the rotor is equally attracted to the nearest stator teeth. The net torque is thus $T_\mathrm{c} = 0$. This is an unstable equilibrium because, at the slightest deflection, the attraction to one of the teeth becomes dominant and cogging torque is produced. As an example, a slight deflection towards 'c' is considered. While moving towards 'c', the torque peaks at its amplitude $T_\mathrm{c} = A_\mathrm{c}$ in position 'b' where the flux takes a path of highest reluctance. To move the rotor further from 'c' to 'd' an actuation torque is required to overcome the cogging torque that tries to pull the rotor back to 'c'. The cogging cycle is completed when position 'd' is reached.

The same cycle repeats for every stable equilibrium position. The cogging torque is thus a periodic signal with a period of $\Delta\theta = 360/n_\mathrm{c}$, with n_c being the number of stable equilibrium positions. This number n_c equals the least common multiple of the number of slots and poles. In the case of the principle 2p4s PMSM, the period equals $\Delta\theta = 90°$. The used PMSM exists of 6 poles and 18 slots, which means that there are 18 equilibrium positions and the mechanical period is $\Delta\theta = 20°$.

2.3. Linearization of the cogging torque

The cogging torque T_c is characterised through static measurements. The rod is put in 1 of the 18 equilibrium positions where the deflection is $\delta\theta = 0°$. For any deflection $\delta\theta$, an actuation torque is required to have static equilibrium: $T_\mathrm{m} = T_\mathrm{c}$.

During a slowly increasing motor torque T_m, the deflection $\delta\theta$ is measured. The rate of change of the torque is set sufficiently low to state that there is no speed and static equilibrium is achieved. The experiment stops when the rod accelerates and static equilibrium is no longer possible. First, the positive direction is characterized and then the negative direction.

The resulting torque-position characteristic is shown in figure 4. Only the peak-to-peak profile (A_c1 to A_c2) can be measured. From the moment the motor torque T_m overcomes the peak A_c, the load accelerates and static equilibrium is no longer possible. It is thus unknown how the profile completes the cogging period of 20°. The torque-position relation is strongly non-linear and not symmetric as shown in figure 3e. In the positive direction, the peak of 25 N mm occurs at 7° and in the negative direction the peak of 23 N mm occurs at −4°.

The cogging stiffness k is calculated as the derivative of the load torque T_l. The result for an increment of 0.2° is shown in figure 4b. The closer to equilibrium, the higher the stiffness.

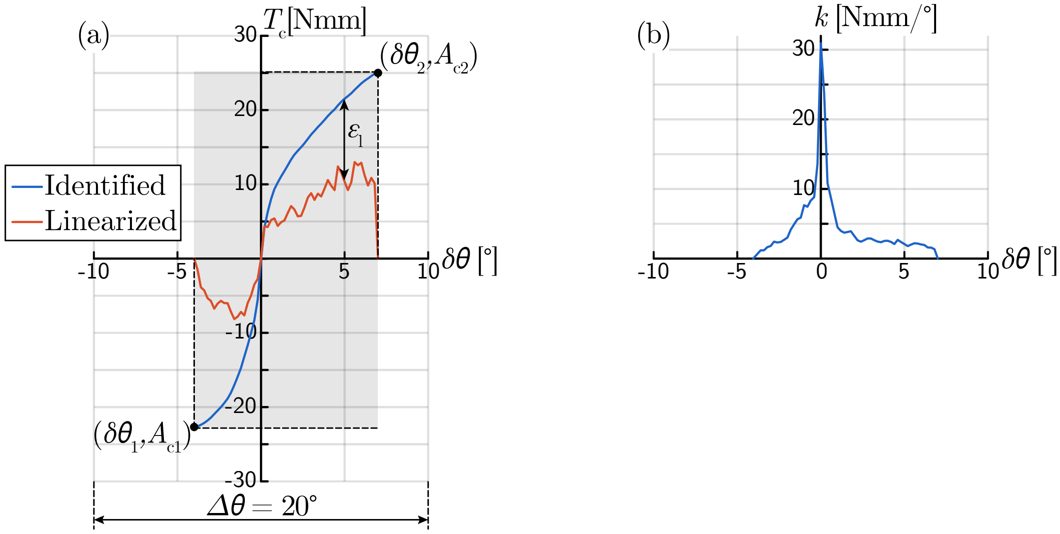

Figure 4: Identified and linearized cogging torque T_c (a) and cogging stiffness k (b).

The proposed frequency-domain tracking technique requires linear system behaviour. The cogging torque T_c is linearized according to the position-dependent cogging stiffness k:

$$T_c(\theta) = k(\theta) \cdot \theta + \varepsilon_l(\theta) \tag{2}$$

In an arbitrary position θ, the cogging torque is modelled as a summation of a linear part $k \cdot \theta$ and the linearization error ε_l. The stiffness k equals the slope of the torque in that position. The linearized part is plotted in figure 4a showing that its validity is limited to small deflections.

Near equilibrium $\delta\theta \approx 0°$, the stiffness reaches its maximum and the linearization error is minimal $\varepsilon_l \approx 0$. Further from equilibrium, the linearisation error increases towards the peak positions. At these positions, the stiffness is $k = 0$, implying that there is no attractive force towards the stable equilibrium which is untrue. An important linearisation condition is thus to keep the deflection small during parameter tracking.

2.4. *Linearized system and initial parameter values*

Substitution of the linearized cogging torque in the motion equation (1) leads to a linear differential equation. Through the Laplace transform, the torque-position transfer function $H_1(s)$ is obtained:

$$H_1(s) = \frac{\theta(s)}{T_m(s)} = \frac{1}{Js^2 + bs + k(\theta)} \tag{3}$$

Note that this transfer function is only valid if the linearization error is negligible $\varepsilon_l \approx 0$. As discussed in section 3, the settings of the stiffness tracker are tuned from initial parameter values. The inertia J is known from the CAD assembly. The stiffness k is characterized in figure 4b but the used method is time-consuming. The stiffness characteristic is therefore not used for obtaining initial guesses but is used for comparison with the tracked stiffness using the developed stiffness tracker.

A user-friendly method is to extract the initial values for the stiffness k and damping b from an impulse response. The mechanism is put in a stable equilibrium position $\delta\theta = 0°$ and is manually actuated with a short tick on the rod. The response is measured and plotted in figure 5.

The plot shows damped oscillations, which is expected for an under-damped second-order system. The plot confirms that stiffness is position-dependent as the period Δt of the oscillations is not constant: $\Delta t_1 \neq \Delta t_2$. The stiffness characteristic in figure 4b shows that the stiffness k increases while the position θ decreases. According to the principle equations below (Brandt, 2011), this means that the period Δt decreases while the position θ decreases as the oscillations damp out:

$$f_\mathrm{n} = \frac{1}{2\pi}\sqrt{\frac{k}{J}} \qquad f_\mathrm{d} = f_\mathrm{n}\sqrt{1-\zeta^2} \qquad \zeta = \frac{b}{2\sqrt{kJ}} \qquad \Delta t = \frac{1}{f_\mathrm{d}} \tag{4}$$

In the above equations, f_n is the natural frequency, f_d is the damped natural frequency, and ζ is the damping ratio. This damping ratio ζ is extracted from the exponential decay σ of the peaks A_1 and A_2 (Brandt, 2011):

$$\sigma = \ln\left(\frac{A_1}{A_2}\right) \qquad \zeta = \frac{\sigma}{\sqrt{\sigma^2 + 4\pi^2}} \tag{5}$$

By substituting the measured values of the impulse response peaks, the damping ratio is found as $\zeta = 0.268$. Substitution of the ratio ζ and given inertia J in (4) leads to an initial value of the damping $b = 0.142\,\mathrm{N\,mm\,s/°}$ and stiffness $k = 12.79\,\mathrm{N\,mm/°}$.

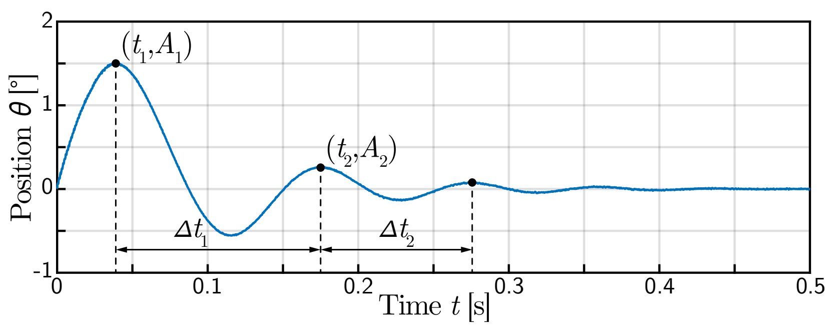

Figure 5: Impulse response measurement

2.5. *Transfer function reduction*

The transfer function scheme of the closed-loop speed controller is shown in figure 6. The different transfer functions are the speed controller $C_\mathrm{s}(s)$, the current controller $C_\mathrm{c}(s)$, the torque-position transfer function $H_1(s)$ and the feedback transfer function $F(s)$. The current controller is

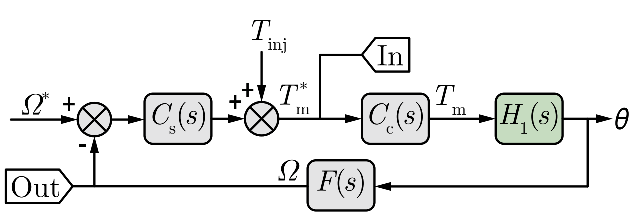

Figure 6: Transfer function scheme of the closed-loop speed controller.

a field-oriented current controller of which the torque-current relation is expressed as (Bu et al., 2021):

$$T_{\mathrm{m}} = \frac{3p}{4}(\psi_f i_q + (L_d - L_q) i_d i_q) \tag{6}$$

In this equation T_{m} is the electromagnetic actuation torque or also called the motor torque, p is the number of poles, ψ_f is the magnetic flux linkage, L_d and L_q are the d-axis and q-axis stator inductance, and i_d and i_q are the d-axis and q-axis stator current. The torque-current relation can be simplified because the rotor of the observed PMSM has surface-mounted magnets, enabling to state $L_d = L_q$. It is further assumed that the magnetic flux linkage ψ_f is a constant machine parameter. As a result, the torque-current relation simplifies to:

$$T_{\mathrm{m}} = K_T i_q \qquad\qquad K_T = \frac{3p}{4}\psi_f = 0.63\,\frac{\mathrm{N\,m}}{\mathrm{A}} \tag{7}$$

It is clear from equation (7) that the motor torque can easily be controlled by the q-axis current i_q, which is generally called the torque-generating current. The factor between the torque and current is called the torque constant K_T. The desired d-axis current is set to $i_d^* = 0$ because this component does not contribute to the actuation torque.

It is generally accepted to simplify the relation between the desired T_{m}^* and actual torque T_{m} as a first-order transfer function with an electrical time constant τ_{e} (Bu et al., 2021):

$$C_{\mathrm{c}}(s) = \frac{T_{\mathrm{m}}(s)}{T_{\mathrm{m}}^*(s)} = \frac{1}{\tau_{\mathrm{e}} s + 1} \tag{8}$$

For a properly tuned current controller, the electrical time constant τ_{e} is much smaller than the mechanical time constant. This allows to state that state that $T_{\mathrm{m}}^* = T_{\mathrm{m}}$ with a negligible error (Pollefliet, 2017). Therefore, T_{m}^* is selected as the input signal for parameter tracking. In figure 6, this signal is marked with "In". An additional advantage of this selection is that measurement noise originating from the current sensor of the q-axis current is automatically excluded.

Using the actual speed Ω as the feedback signal, the desired speed Ω^* is regulated with a classic PI-controller $C_{\mathrm{s}}(s)$:

$$C_{\mathrm{s}}(s) = \frac{\Omega(s)}{\Omega^*(s)} = K_{\mathrm{p}}\left(1 + \frac{K_{\mathrm{i}}}{s}\right) \tag{9}$$

The actual speed Ω is computed as the derivative of the actual position θ. The position is measured with a built-in encoder. To suppress high-frequency noise due to discrete derivation, a low-pass filter is added resulting in the feedback transfer function $F(s)$:

$$F(s) = \frac{\Omega(s)}{\theta(s)} = \frac{s}{\tau s + 1} \tag{10}$$

The time constant $\tau = 1$ ms is tuned to have a cut-off frequency of about 160 Hz. Multiplying the torque-position transfer function $H_1(s)$ in (3) with $F(s)$ results in the torque-speed transfer function $H_2(s)$:

$$H_2(s) = \frac{\Omega(s)}{T_{\mathrm{m}}(s)} = \frac{s}{(Js^2 + bs + k(\theta))(\tau s + 1)} \tag{11}$$

Because of the inherent noise suppression using the filter in $F(s)$, the actual speed Ω is selected as the output signal for parameter tracking. The signal is marked with "Out" in figure 6. With T_m being the input and Ω being the output, the torque-speed transfer function $H_2(s)$ is the selected model for parameter tracking.

As discussed in section 3, an additional torque signal T_{inj} is injected to enable parameter tracking. This signal ensures that the frequency content at the tracking frequencies is sufficiently high. The relevant transfer functions are defined as:

- The closed-loop transfer function $G_1(s)$:

$$\begin{aligned} G_1(s) = \frac{\Omega(s)}{\Omega^*(s)} &= \frac{C_s(s)H_2(s)}{1 + C_s(s)H_2(s)} \\ &= \frac{K_p(s + K_i)}{J\tau s^3 + (J + b\tau)s^2 + (b + k\tau + K_p)s + k(\theta) + K_p K_i} \end{aligned} \tag{12}$$

- The transmission transfer function $G_2(s)$:

$$\begin{aligned} G_2(s) = \frac{T_m(s)}{T_{inj}(s)} &= \frac{1}{1 + C_s(s)H_2(s)} \\ &= \frac{(\tau s + 1)(J s^2 + bs + k(\theta))}{J\tau s^3 + (J + b\tau)s^2 + (b + k(\theta)\tau + K_p)s + k(\theta) + K_p K_i} \end{aligned} \tag{13}$$

Tuning of the speed control settings is based on the high-speed requirements when the mechanism is operational. Setting the closed-loop bandwidth of $G_1(s)$ to 10 Hz allows fast and robust operation. Using the magnitude of (12) and the objective of having a closed-loop bandwidth of 10 Hz, K_p and K_i are tuned using a trial and error approach. Their values are listed in table 1 and are used for simulations and measurements.

When parameter tracking is desired, the injected torque T_{inj} is added with the speed controller activated. This ensures limited machine task interruption. Consequently, the controller manipulates the injected torque T_{inj} and tuning is required through the transmission transfer function $G_2(s)$ for achieving sufficient signal content at the tracking frequencies. This tuning procedure is discussed in the next section 3.

3. Using SDFT for stiffness tracking

3.1. Magnitude tracking

The proposed SDFT technique is shown in figure 7 and consists of two parts: magnitude tracking and parameter conversion. In the first part, the SDFT algorithm is used for tracking the amplitudes of the input signal and output signal at the injected tracking frequencies f_i. The tracked magnitudes M_i are the ratio of the tracked output amplitudes $|\Omega|_i$ over the tracked input amplitudes $|T_m|_i$.

The SDFT takes advantage of its sliding property by computing each new $N-$point DFT at time instance n from the $N-$point DFT of one sample earlier $(n - 1)$ using the circular shift property (Jacobsen and Lyons, 2003). Because a new DFT is not calculated from scratch every time, the

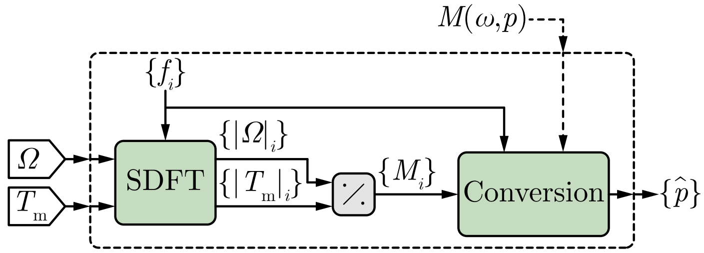

Figure 7: General parameter tracking approach.

SDFT is a computationally efficient and recursive algorithm for calculating the Fourier components $\mathcal{F}[x]_h$ of a given signal $x(n)$ based on N samples (Liu et al., 2018):

$$\mathcal{F}[x]_h(n) = \frac{1 - z^{-N}}{1 - e^{j(2\pi/N)h}} \frac{1}{N} x(n) \qquad h_i = \{h_1; h_2; ...; h_l\} \tag{14}$$

In this equation, N equals the number of samples of the fundamental component and h_i is the harmonic pattern. The pattern is an array of integer multiples of the fundamental component $h_1 = 1$. The implementation of (14) is shown in figure 8 for the signal $x(n)$. The SDFT can be configured to match with a user-defined harmonic pattern. For each harmonic, one bin is added. For a pattern of l harmonics, the SDFT requires $2 \cdot l \cdot N$ additions and $l \cdot N$ multiplications. With the multiplications being the mathematical operation requiring the most effort, the computational complexity is found as $\mathcal{O}(l \cdot N)$. This is much more computationally efficient than using the DFT having a computational complexity of $\mathcal{O}(N^2)$ (Rafii, 2018).

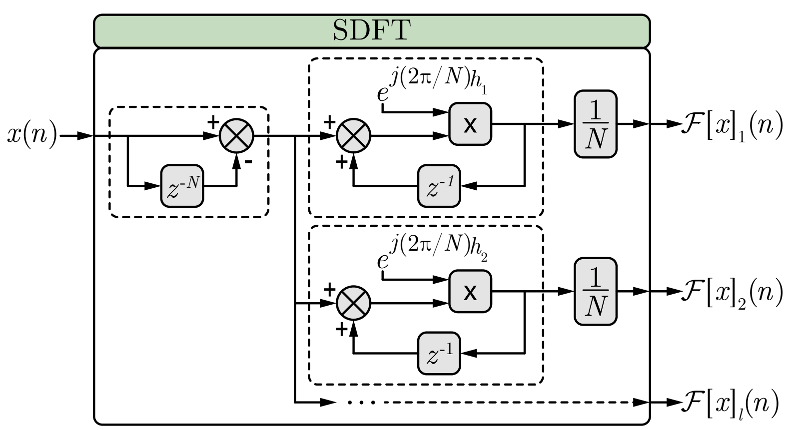

Figure 8: Implementation of the SDFT algorithm.

The used signals are in this case the motor torque T_m and the actual speed Ω. The amplitude of each frequency $f_i = f_1 \cdot h_i$ is found from the real and imaginary part of their Fourier component:

$$\begin{aligned} |\Omega|_i &= \sqrt{\Re(\mathcal{F}[\Omega]_h)^2 + \Im(\mathcal{F}[\Omega]_h)^2} \\ |T_\mathrm{m}|_i &= \sqrt{\Re(\mathcal{F}[T_\mathrm{m}]_h)^2 + \Im(\mathcal{F}[T_\mathrm{m}]_h)^2} \end{aligned} \tag{15}$$

Before having valid tracked amplitudes and magnitudes, the initial SDFT-window must be filled with data. The shifting time window δt of is determined by the fundamental frequency f_1:

$$\delta t = \frac{1}{f_1} \qquad\qquad N = \frac{\delta t}{t_s} = \frac{1}{f_1 t_s} \tag{16}$$

This initialisation is taken into account by including a delay before the parameter conversion starts.

The first part of the SDFT technique relies on the accurate reproduction of discrete signals to their continuous equivalent. Discrete signals are known to be prone to leakage, quantisation and noise.

By injecting a leakage-free harmonic spectrum and configuring the SDFT accordingly, leakage is fully suppressed. A spectrum is free from leakage if the fundamental frequency f_1 and all its harmonics have an integer-valued window size. Using equation (16), an array of fundamental frequencies f_1 resulting in integer values for the window size N is found. The sample time t_s = 250 µs is fixed to the configured one of the provided motion controller. Once the fundamental frequency f_1 is selected, the harmonic pattern h_i is limited to the ones resulting in integer-valued sizes of their accompanying period. For example $f_1 = 1$ Hz is leakage-free because the window size equals $N = 40000$. The second harmonic $h = 2$ has a period $N/2 = 20000$ which is also leakage-free, but the third $h = 3$ is not because one $N/3$ is a non-integer value.

The effect of quantisation and noise is studied after discussing the guidelines for tuning the injection signal T_{inj}.

The used control scheme for parameter tracking is shown in figure 9. As concluded in the previous section, the deflection around equilibrium must be small to have a negligible linearisation error. The control strategy is therefore set to first move to the equilibrium position $\theta = 0°$. Then, the speed is set to $\Omega^* = 0$ and the injection torque T_{inj} is enabled. This ensures to have motion around equilibrium (Vanbecelaere et al., 2019).

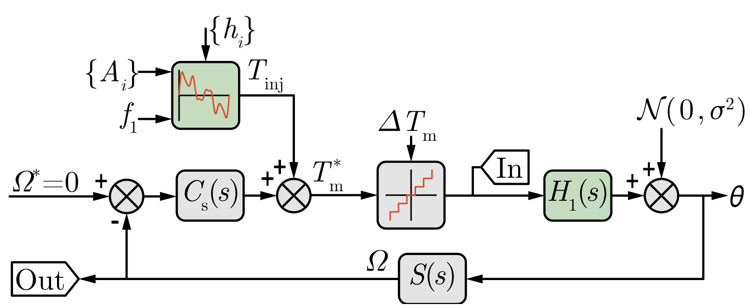

Figure 9: Control scheme expanded with multi-sine injection for parameter tracking.

The injected signal T_{inj} is defined as a multi-sine containing the tracking frequencies f_i:

$$T_{inj} = \sum_{i=1}^{l} [A_i \sin(2\pi f_i t + \varphi_i)] \tag{17}$$

Tuning T_{inj} involves selecting the tracking frequencies f_i and their accompanying amplitudes A_i and optionally their phases φ_i. The tuning is based on a trade-off between limiting the linearisation and quantization error. As shown in the control scheme in figure 9, the input torque T_m is quantized with an interval of ΔT_{m}. The interval is fixed and is determined by the resolution of the torque generating current i_q of 1 mA. According to (7), this gives an interval of $\Delta T_{\mathrm{m}} = 0.63\,\mathrm{N\,mm}$.

Setting the amplitudes A_i high leads to a high number of increments in the torque signal T_{m} and a limited quantization error ε_{q}. But the higher the amplitudes A_i, the higher the deflection $\delta\theta$ and the higher the linearization error ε_{l}.

To find a feasible trade-off, the magnitudes of the torque-position transfer function $|H_1(s)|$ and transmission transfer function $|G_2(s)|$ are plotted in figure 10. The plots are achieved by substituting the initial guesses of the stiffness $k = 12.79\,\mathrm{N\,mm/^\circ}$ and damping $b = 0.142\,\mathrm{N\,mm\,s/^\circ}$ in equations (3) and (13) for frequencies from $f = 0$ to 20 Hz. The other parameters J, τ, K_p, K_i are known constants. The f-axis is set to the leakage-free candidates. The frequencies f_i and accompanying amplitudes A_i are selected based on the following guidelines:

- All frequencies are selected in a range where the stiffness significantly affects the dynamics. The magnitude $|H_1(s)|$ for $k, b = 0$ is plotted in figure 10a. The higher the frequency, the less the stiffness affects the dynamics.

- The number of tracking frequencies is limited to $l = 5$. The more data points l, the more the potential errors on the tracked magnitudes are suppressed. But more tracking frequencies also lead to a higher deflection amplitude $|\delta\theta|$ and consequently a higher linearisation error ε_{l}. Moreover, in the next subsection where the parameter conversion algorithm is introduced, limiting the number of tracking frequencies is also required to limit the computational complexity.

- To keep the deflection low $\delta\theta \approx 0$, the deflection amplitude $|\delta\theta|_i$ caused by each harmonic f_i is limited. This amplitude $|\delta\theta|_i$ equals:

$$|\delta\theta|_i = A_i \cdot |G_2(s)|_i \cdot |H_1(s)|_i \tag{18}$$

  Independent of the assigned amplitude A_i, it is avoided to select frequencies f_i close to resonance.

- Through simulations using the control scheme in figure 9, it is found that 10 increments of the input signal T_{m} is sufficient to have a negligible quantisation error ε_{q}. This is guaranteed by assigning 10 increments to the individual amplitudes $|T_{\mathrm{m}}|_i$. To do so, the amplitudes A_i must respect the following condition for the given interval of $\Delta T_{\mathrm{m}} = 0.63\,\mathrm{N\,mm}$:

$$A_i \cdot |G_2(s)|_i \geq 6.3\,\mathrm{N\,mm} \tag{19}$$

An example of the tuning procedure is given for clarification. The candidates $f_i = 5\,\mathrm{Hz}$ and $f_i = 10\,\mathrm{Hz}$ are compared. Figure 10a shows that the leakage-free candidate $f_i = 5\,\mathrm{Hz}$ has a torque-position magnitude of $|H_1|_i = 2.03$ and a transmission magnitude of $|G_2|_i = 0.22$. According to (19) the injected amplitude is found as $A_i = 29\,\mathrm{N\,mm}$ for having at least 10 increments. With this amplitude A_i, the deflection amplitude is found using (18) as $|\delta\theta|_i = 0.74^\circ$. This candidate is not selected because selecting $f_i = 10\,\mathrm{Hz}$ leads to only $|\delta\theta|_i = 0.50^\circ$ for the same amount of 10 increments in the actuation torque. The lower the deflection, the lower the linearisation error.

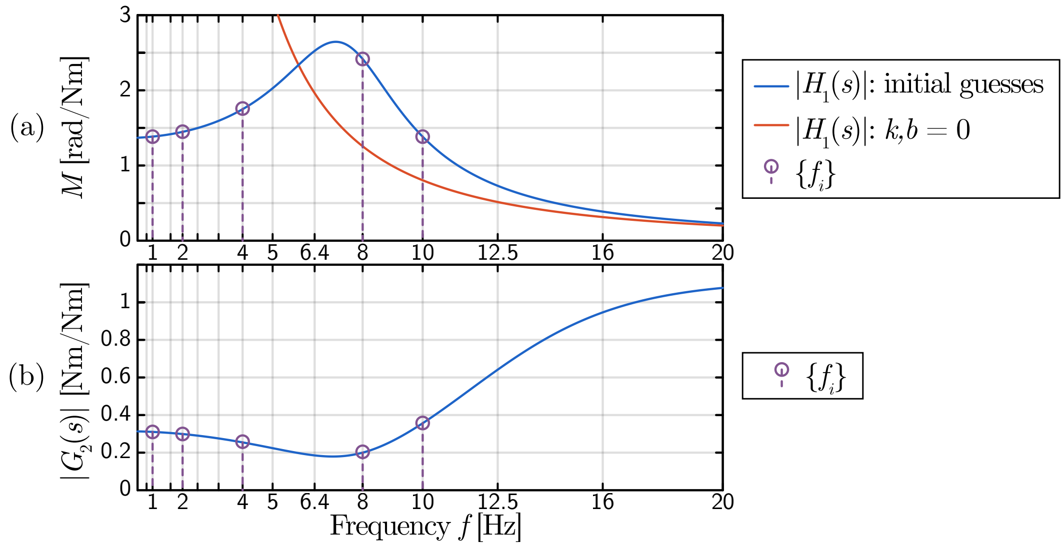

Figure 10: Selection of the tracking frequencies f_i based on the torque-position magnitude (a) and transmission magnitude (b).

Using the control scheme in figure 9, the effect of quantisation and noise on the tracked magnitudes is investigated. The model is set to the transfer function $H_1(s)$ with the parameter values fixed to the known constants and the initial guesses of the stiffness and damping. Not only the input torque is quantized, but also the actual position θ. Based on the encoder specifications, the position is quantised with an interval of $^{360°}/_{2^{20}}$. This interval is not included in the simulation because the effect is negligible. By measuring the position θ at rest for a long time, it is found that normally distributed noise $\mathcal{N}$ affects the actual position θ. A mean value $\mu = 0$ rad and a standard deviation of $\sigma = 0.0001$ rad is determined and included in the control scheme.

Using the proposed guidelines, the tracking frequencies f_i and A_i are set to the ones listed in table 1. With these settings, the tracked magnitudes are nearly exact. To have a clear effect of the potential errors, the tracked magnitudes M_i in figure 11a are presented with the amplitudes A_i set 10 times lower and the standard deviation σ set 5 times higher. It can be observed that the settling time t_{set} is larger than the time window δt of SDFT. The tracked magnitudes only correspond with the actual ones after settling.

The distribution of the tracked magnitude M_4 is plotted in figure 11b showing a normal distribution. Normally distributed noise thus leads to normally distributed tracked magnitudes with a standard deviation σ_ε and mean μ_M. In the case of M_4 the relative standard deviation equals $\sigma_\varepsilon = 0.65\,\%$ for an absolute standard deviation of the noise on the position θ of $\sigma = 0.0005$ rad. Due to the quantization, the tracked mean μ_M differs from the actual magnitude. In the case of M_4 the quantization error equals $\varepsilon_{\text{q}} = 0.06\,\%$ for an actuation torque T_{m} having 6 increments.

In general, it can be concluded that quantization causes a constant error on the tracked magnitudes and noise causes a normally distributed error on top of it. With the proposed control scheme for parameter tracking in figure 9 and the presented guidelines, the potential errors are sufficiently suppressed. Note that the effect of the linearization error is not yet investigated. This is provided in section 4 containing measurements on the experimental setup.

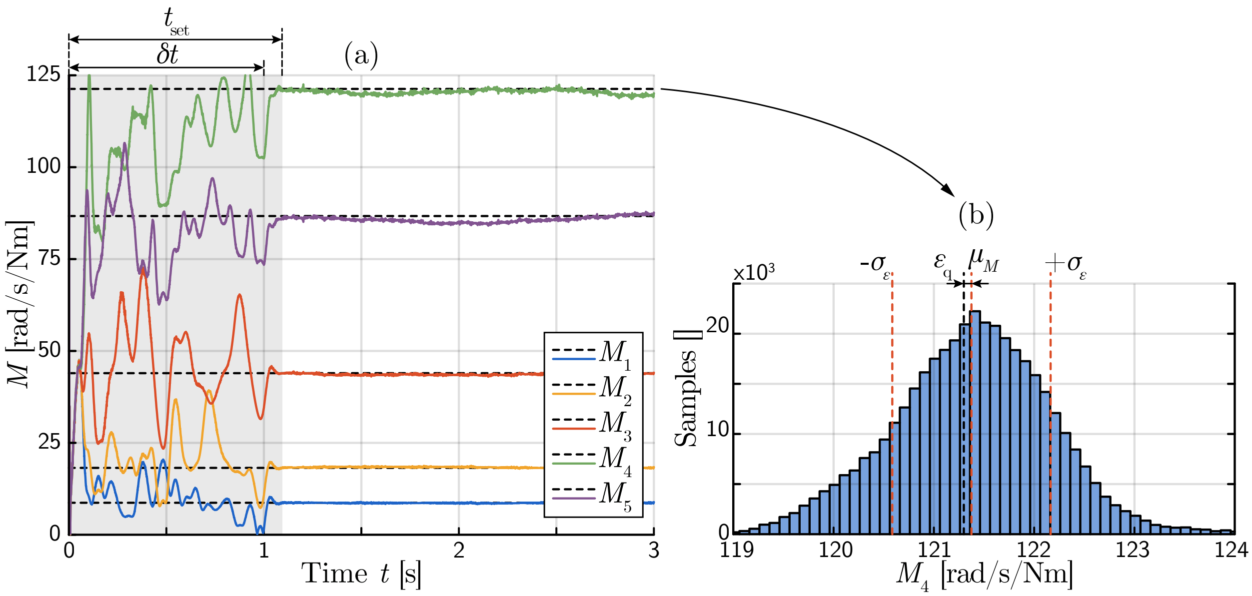

Figure 11: Tracked and actual magnitudes in the presence of noise and quantization (a); Distribution of the tracked magnitude M_4 (b).

3.2. Parameter conversion

As shown in figure 7, the second part of the SDFT technique is parameter conversion where the tracked magnitudes M_i are converted to the tracked parameters $\hat{p}$. This part requires a parameterized function of the magnitude. In this case, the transfer function $H_2(s)$ is selected as the system model. Substitution of $s = j\omega$ in (11) and computing the modulus leads to the parametric magnitude function $M(\omega, p)$:

$$M(\omega, p) = \frac{\omega}{\sqrt{((J + b\tau)\omega^2 - k)^2 + (J\tau\omega^2 - b - k\tau)^2\omega^2}} \tag{20}$$

In this magnitude function, the independent variable is the frequency $\omega = 2\pi f$ and the parameters are collected with the symbol p. The known constants are the inertia J and time constant τ. The unknowns are the damping b and stiffness k. Inspection of the function shows that the magnitude is not linear in its parameters b and k. This means linear algebra cannot be applied. Non-linear curve-fitting techniques are required.

The objective function $f_{\min}$ for curve-fitting techniques equals the least-squares error between the measured and estimated values according to the curve-fit function. In this case, the measured value is the tracked magnitude M_i at frequency $\omega_i = 2\pi f_i$ and the estimated value is the value $M(\omega, p)$ found by substituting the initial or estimated parameters $\hat{p}$:

$$f_{\min} = \sum_{i=1}^{l} [M_i - \hat{M}(\omega_i, \hat{p})]^2 \tag{21}$$

The summation goes up to the number of harmonics l. An iterative algorithm minimizes the least-squares error through a sequence of well-chosen updates of the parameter values. The most common algorithms for non-linear curve-fitting are the gradient descent algorithm, the

Gauss-Newton algorithm (GN) and the Levenberg-Margaurdt algorithm. A comparison between their performance is made in (Gavin, 2013) where it is concluded that the fastest convergence is achieved with GN for small-size problems. Because fast parameter tracking is one of the main objectives, GN is selected for implementation.

The update algorithm of GN assumes that the objective function $f_{\min}$ is approximately quadratic in the parameters p near the solution at its minimum value (Gavin, 2013). This approximation requires the calculation of the gradients of the objective function with respect to the parameters. The gradients are calculated from the partial derivatives and are collected in the Jacobian matrix $\mathbf{J}$:

$$\mathbf{J} = \begin{bmatrix} \dfrac{\partial \hat{M}(\omega_1, \hat{p})}{\partial b} & \dfrac{\partial \hat{M}(\omega_1, \hat{p})}{\partial k} \\ \dfrac{\partial \hat{M}(\omega_2, \hat{p})}{\partial b} & \dfrac{\partial \hat{M}(\omega_2, \hat{p})}{\partial k} \\ \vdots & \vdots \\ \dfrac{\partial \hat{M}(\omega_l, \hat{p})}{\partial b} & \dfrac{\partial \hat{M}(\omega_l, \hat{p})}{\partial k} \end{bmatrix} \tag{22}$$

The partial derivatives with respect to the parameters p are calculated analytically from the magnitude function in (20):

$$\frac{\partial \hat{M}(\omega, \hat{p})}{\partial b} = \frac{-b\tau^2\omega^5 - b\omega^3}{(J^2\tau^2\omega^6 + (J^2 - 2Jk\tau^2 + b^2\tau^2)\omega^4 + (b^2 - 2Jk + k^2\tau^2)\omega^2 + k^2)^{3/2}} \tag{23}$$

$$\frac{\partial \hat{M}(\omega, \hat{p})}{\partial k} = \frac{-k\tau^2\omega^3 + J\omega^3 - k\omega}{(J^2\tau^2\omega^6 + (J^2 - 2Jk\tau^2 + b^2\tau^2)\omega^4 + (b^2 - 2Jk + k^2\tau^2)\omega^2 + k^2)^{3/2}} \tag{24}$$

Using the Jabobian matrix, the update algorithm of GN for computing the updated parameters $\hat{p}_{r+1}$ for the next iteration $r + 1$ from the current ones $\hat{p}_r$ at iteration r is given as (Gavin, 2013):

$$\begin{Bmatrix} \hat{b} \\ k \end{Bmatrix}_{r+1} = \begin{Bmatrix} \hat{b} \\ k \end{Bmatrix}_{r} - \left[\left[[\mathbf{J}_r^T \mathbf{J}_r]^{-1} \right] \mathbf{J}_r^T \right] \left[\begin{Bmatrix} M_1 \\ M_2 \\ \vdots \\ M_l \end{Bmatrix} - \begin{Bmatrix} \hat{M}_1 \\ M_2 \\ \vdots \\ M_l \end{Bmatrix} \right] \tag{25}$$

In order to start the iterations, initial guesses $\hat{p}_0$ must be provided. The algorithm stops when the number of iterations r reaches a configured maximum $r_{\max}$.

For the selected pattern shown in figure 10, the objective function in (21) is graphically visualized in figure 12a for stiffness k and damping b values varying around the actual values. The initial guesses $\{k_0; b_0\}$ are set to the ones identified from the impulse response and are given in table 1. The actual values are set at $k = k_0/2 = 6.40\,\mathrm{N\,mm/^\circ}$ and $b = 1.5b_0 = 0.213\,\mathrm{N\,mm\,s/^\circ}$. The 3D-plot proves that the optimisation problem is convex implying that any initial guess $\{k_0; b_0\}$ leads to convergence towards the solution at the minimum least-squares error. In figure 12b, a contour plot of the objective function is given where the convergence is visualized. From the initial guesses at $r = 0$, the parameters are iteratively updated with steps in the direction of the gradients of $f_{\min}$. At $r = 3$ the actual parameters are found where the least-squarer error equals $f_{\min} = 0$.

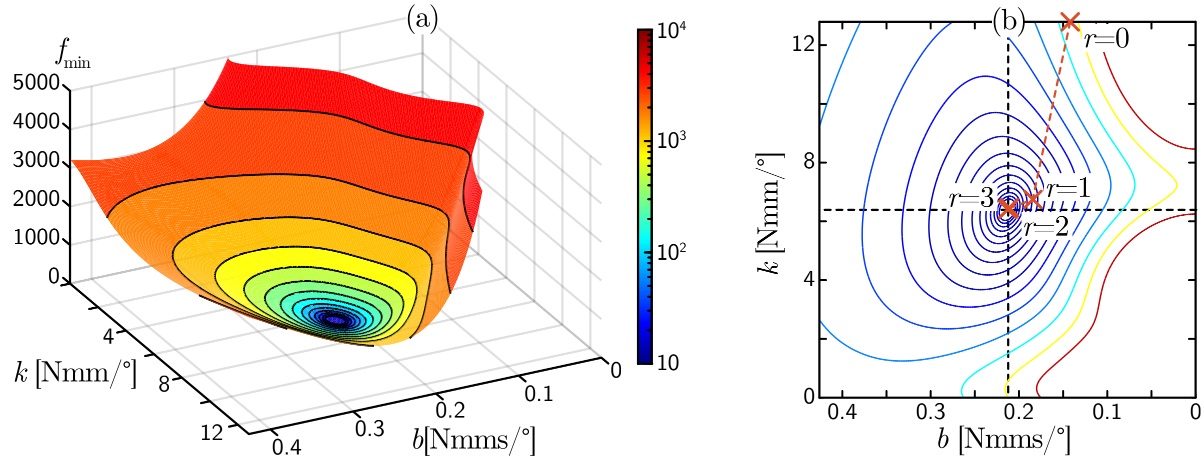

Figure 12: Graphical visualization of the objective function (a) and a contour-plot (b).

3.3. Tracking performance

The implementation of the proposed stiffness tracker is shown in figure 13. As discussed in the introduction, the objective is to track fast changes. The performance of the stiffness tracker is analyzed using the control scheme in figure 9. The model is the torque-position transfer function $H_1(s)$. The actual damping b is set as a constant. The actual stiffness k is set to change over time with a slower rate of change of $\delta k = 1\,\mathrm{N\,mm\,s/^\circ}$ and a faster rate of change of $\delta k = -2\,\mathrm{N\,mm\,s/^\circ}$. The quantization and noise are excluded to focus solely on the tracking performance.

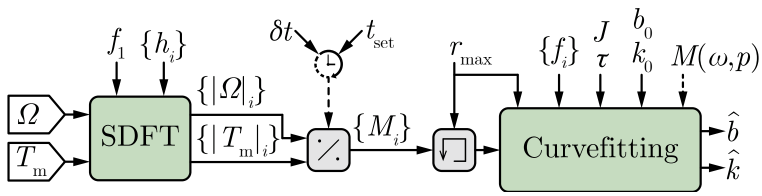

Figure 13: Implementation of the stiffness tracker.

With the tracking settings listed in table 1, the tracked damping $\hat{b}$ and stiffness $\hat{k}$ are shown in figure 14a. The time is set to $t = 0\,\mathrm{s}$ after initialization. The first update from the initial guesses b_0, k_0 to the first estimates $\hat{k}, \hat{b}$ is shown in figure 14b. The set maximum number of iterations $r_{\max} = 5$ is sufficient for reaching convergence. After 5 iterations, the tracked parameters are updated with the iterative estimates $\hat{b}_r, \hat{k}_r$ at $r = 5$. This means that the parameter update time equals $t_p = t_s \cdot r_{\max} = 1.25\,\mathrm{ms}$. At each parameter update, the tracked parameters are set to the initial ones for the next iterations.

After the first parameter update, the tracked stiffness $\hat{k}$ follows the trend of the actual stiffness k but with a tracking error ε_p depending on the rate of change δk. The zoom-in plots in figures 14c and 14d show that the mean tracking error equals $\varepsilon_p = \delta k/2$. The faster the stiffness changes, the higher the error.

The tracking error ε_p originates from using a sliding window. The parameters are computed from the past N samples of the sliding window. Because the stiffness changes within the time window $\delta t = 1\,\mathrm{s}$, the actual value cannot be tracked. A value close to the mean value is tracked

Table 1: Settings of the stiffness tracker.

Controller	$\tau = 0.001\,\mathrm{s}$
	$K_\mathrm{i} = 0.02\,\mathrm{N\,m\,s/rad}$
	$K_\mathrm{p} = 80/\mathrm{s}$
Known inertia	$J = 315\,\mathrm{kgmm}^2$
Initial guesses	$b_0 = 0.142\,\mathrm{N\,mm\,s}/^\circ$
	$k_0 = 12.79\,\mathrm{N\,mm}/^\circ$
Harmonic pattern	$f_1 = 1\,\mathrm{Hz}$
	$h_i = \{1; 2; 4; 8; 10\}$
	$A_i = \{21; 22; 25; 32; 18\}\,\mathrm{N\,mm}$
Update	$t_\mathrm{init} = 1.2\,\mathrm{s}$
	$r_\mathrm{max} = 5$

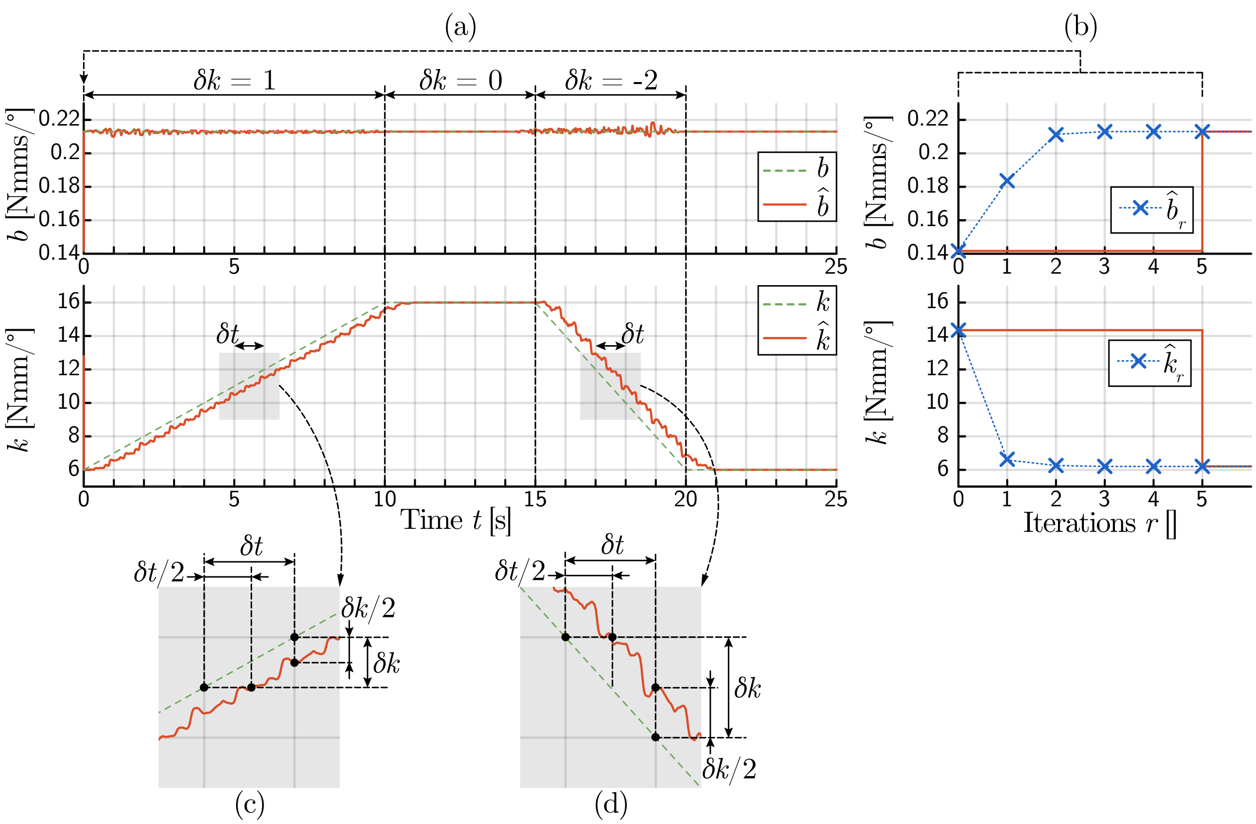

Figure 14: Tracked stiffness $\hat{k}$ and damping $\hat{b}$ compared to the actual values (a); first iterations during curve-fitting (b); zoom-in of the tracked stiffness at the slower stiffness change (c) and faster stiffness change (d).

instead. In this case of a constant rate of change δk, the mean tracking error equals $\varepsilon_p = \delta k/2$. Consequently, the tracked stiffness lags with $\delta t/2$. The time window δt must be small to suppress this tracking error. According to (16) this means that the fundamental frequency f_1 must be set high but figure 10a shows that the tracking frequencies f_i are bounded to a low range where the stiffness affects the dynamics. Selecting f_1 thus determines the rate of change δk of the stiffness that can be tracked. The mean error ε_p is proportional to:

$$\varepsilon_p = \frac{\delta k}{2\delta t} = \frac{\delta k}{2} f_1 \tag{26}$$

Figure 14a further shows that when both parameters are constant, the tracked parameters are exact. Note that the simulations only consider the potential tracking error due to using a sliding window. In the next section, the developed stiffness tracker is validated on the experimental setup where the other potential errors namely linearization, quantization and noise are present.

4. Measurements

4.1. Validation of the proposed stiffness tracker

The proposed stiffness tracker is validated by tracking the cogging stiffness and damping of the PMSM-driven rod in figure 2. The identified cogging stiffness in figure 4b is used as a reference for comparing with the tracked stiffness. The real-time controller is configured in torque mode and runs on a commercially available industrial PC at a sample time of $t_s = 250\,\mu$s. The motion controller and tracking scheme shown in figure 13 are developed in Matlab/Simulink and implemented on the real-time control platform using the provided *code generation* toolbox.

The tracking settings are listed in 1 but some are adapted. Because stiction is observed during experimentation, the amplitudes A_i are set higher: $A_i = \{50; 50; 50; 13; 8\}$ N mm. To compensate for the increased deflection $\delta\theta$, the phases φ_i are shifted: $\varphi_i = \{15°; 5°; 45°; 80°; 90°\}$ N mm. Note that the deflection must be limited to suppress the linearization error.

The measured control signals are plotted in figure 15 for 2 periods of the injected multi-sine. The initial one is not shown because it is used for initializing the SDFT. The injected torque T_{inj}

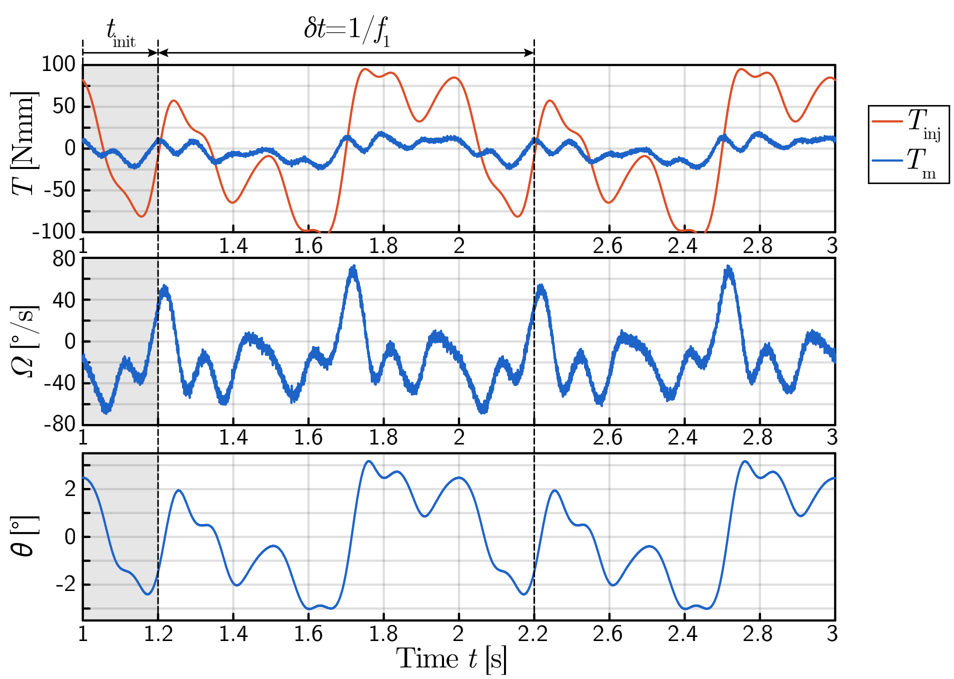

Figure 15: Injected torque T_{inj}, desired torque T_{m}, actual speed Ω and actual position θ during parameter tracking.

is manipulated by the speed controller leaving the desired torque T_{m} for actuation. The desired frequency content is sufficiently present. The actual speed Ω and position θ contain the desired periodicity of $1/f_1$. The deflection is limited to about 3° in both directions.

Combining the position-dependent cogging stiffness $k(\theta)$ plotted in figure 4b with the measured position $\theta(t)$ leads to the time-dependent cogging stiffness $k(t)$ plotted in figure 16. The stiffness strongly changes within the sliding time window δt. As concluded in the previous section, only the mean value $\mu_k = 5.32\,\mathrm{N\,mm}/°$ can be tracked. The mean μ_k is therefore used as the reference for validation.

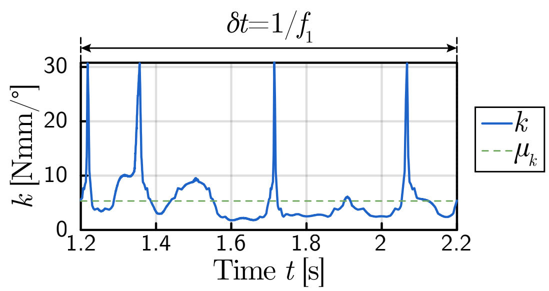

Figure 16: Time-dependent cogging stiffness k for 1 time window and its mean μ_k.

The amplitudes $|T_{\mathrm{m}}|_i$ and $|\Omega|_i$ at the harmonic spectrum h_i are tracked using SDFT and plotted in figure 17. The amplitudes are nearly constant indicating that noise is not an issue and that quasi-linear system behaviour is achieved. The quantization error is however not negligible because the amplitudes $|T_{\mathrm{m}}|_4$ and $|T_{\mathrm{m}}|_5$ violate the condition in (19) of being at least $6.3\,\mathrm{N\,mm}$. This is because the tuning T_{inj} is performed with initial guesses of the stiffness k_0 and damping b_0 which deviate from the actual values.

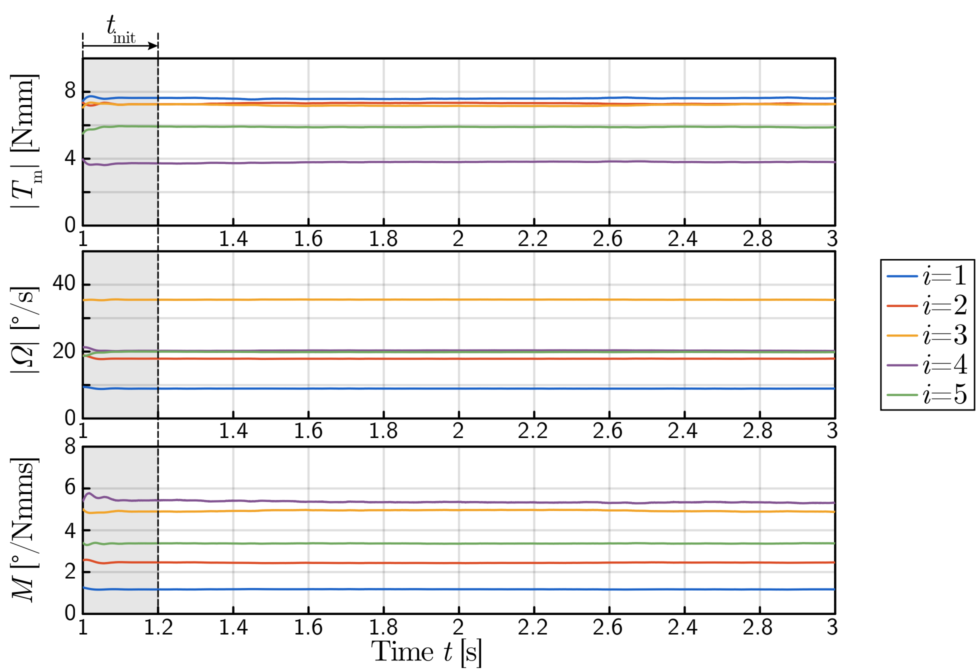

Figure 17: Amplitudes of the torque T_{m} (top), speed Ω (middle), and magnitude M at the selected harmonics h_i.

After the initialization time t_{init}, steady-state is reached and the tracked magnitudes M_i are used for parameter conversion with the curve-fitting algorithm.

Using the GN algorithm, the tracked magnitudes are converted to the tracked parameters. The tracked stiffness $\hat{k}$ and damping $\hat{b}$ are plotted in figure 18. The tracked damping $\hat{b}$ shows a slowly decreasing trend. The tracked cogging stiffness $\hat{k}$ remains constant for this tracking time of 10 s. Compared to the reference μ_k, the mean tracking error is $\varepsilon_p = 32\,\%$. The inevitable trade-off between the linearization and quantization error is the main cause of this deviation. In the next subsection, a benchmark with the Welch technique is made for evaluating the accuracy.

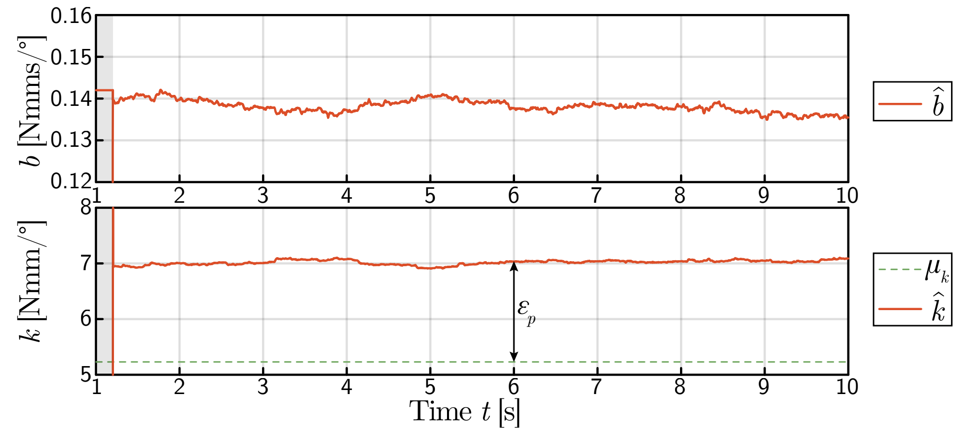

Figure 18: Tracked cogging stiffness $\hat{k}$ and damping $\hat{b}$ of the PMSM-driven rod.

The robustness of the curve-fitting algorithm is illustrated in figure 19 for the initial parameter update at $t = 1.2$ s. The initial magnitude $\hat{M}_0$ at $r = 0$ converges to the estimated magnitude $\hat{M}$ at $r = 5$. A clear fit with the tracked magnitudes M_i is found. The least-squares fit however does not equal $f_{\min} = 0$ because of the tracking errors. The least suppressed one is the linearization error. Despite the errors, the stiffness tracker provides feasible estimates proving its robustness.

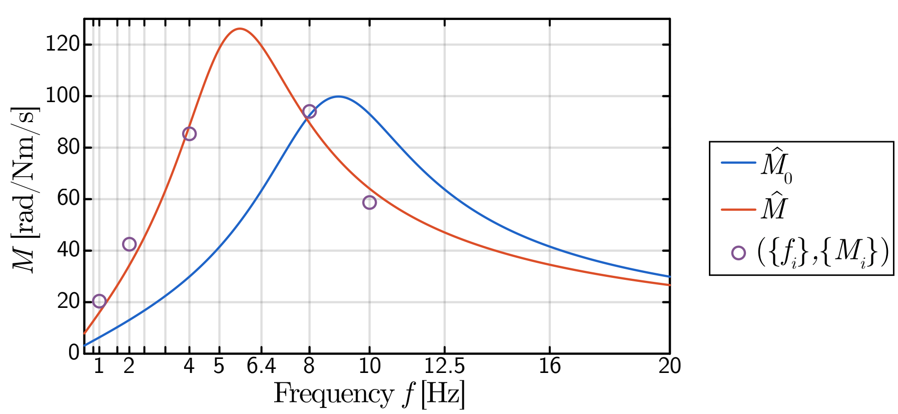

Figure 19: Tracked magnitudes M_i, initial magnitude function $\hat{M}_0$ and final magnitude function $\hat{M}$.

Based on the experimental results, it can be concluded that the proposed SDFT technique for stiffness tracking is successfully implemented on a commercially available real-time motion controller. A mean tracking error of $\varepsilon_p = 32\,\%$ is obtained in an update time of only $t_p = 1.25\,\text{ms}$. Due to the use of a sliding window of $\delta t = 1\,\text{s}$, the mean of the changes within this window is tracked.

4.2. Benchmark with the Welch technique

The classic off-line frequency-domain technique for parameter estimation is the Welch technique (Villwock and Pacas, 2008) and is bench-marked against the proposed on-line SDFT technique. The Welch technique uses noise injection to identify the magnitude characteristic at a broad range of frequencies. Thereafter, some of the magnitudes are manually selected for parameter conversion.

The injected torque T_{inj} is defined as a random sequence of values between a specified maximum T_{max} and minimum $-T_{\text{max}}$. All values in between have the same probability of being selected. The resolution Δf of the frequency content is determined by the measurement time. The higher the measurement time, the finer the resolution Δf. Consequently, many non-periodic frequencies are present leading to leakage. The Welch technique suppresses leakage through averaging with window techniques.

The same control strategy as with the SDFT technique is used. Only now the injected torque T_{inj} is replaced by the noise with a maximum of $T_{\text{max}} = 140\,\text{N\,mm}$. For leakage suppression and having a fine resolution, the measurement time is set to have at least 100s of data. The number of windows is set to $w = 32$ each having $50\,\%$ overlap. The measured torque-speed magnitude characteristic is shown in figure 20 and is achieved using the *tfestimate*-function in Matlab which consists of the Welch algorithm. During the measurement, the maximum deflection is 6°.

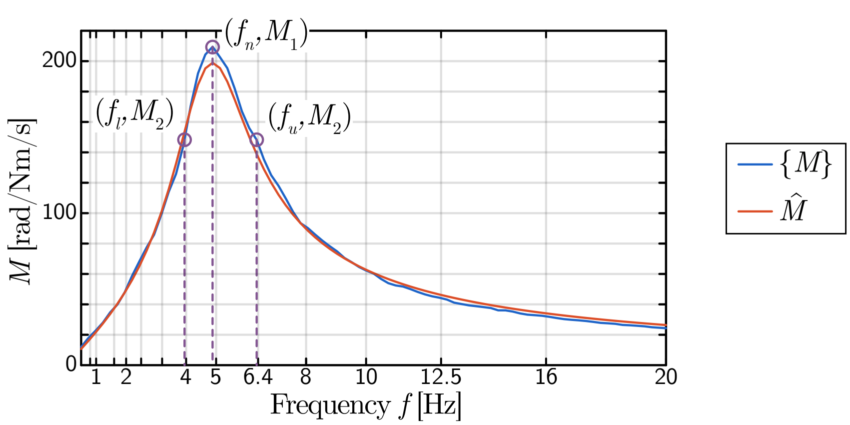

Figure 20: Identified magnitudes $\{M\}$ using Welch and estimated magnitude $\hat{M}$ using peak picking with the selected coordinates indicated.

Rather than using the non-linear curve-fitting algorithm with the whole magnitude vector $\{M\}$ as data points, the peak picking method is suggested (Brandt, 2011) where the user selects 3 feasible coordinates inside the resonance peak:

- Select M_1 at the natural frequency f_n.

- Calculate $M_2 = \dfrac{M_1}{\sqrt{2}}$.

- At M_2, select the lower frequency $f_l < f_n$ and the upper frequency $f_u > f_n$.

From these coordinates, first principle formulas allow estimation of the stiffness $\hat{k}$ and damping $\hat{b}$ (Brandt, 2011):

$$k = (2\pi f_n)^2 J \qquad\qquad b = 2\pi \frac{f_u^2 - f_l^2}{f_n} J \tag{27}$$

Substituting the 3 selected coordinates in (27), the estimated stiffness is found as $\hat{k} = 5.17\,\mathrm{N\,mm/^\circ}$ and the damping as $\hat{b} = 0.18\,\mathrm{N\,mm\,s/^\circ}$. Substituting these values in (20) leads to the estimated magnitude function $\hat{M}$ plotted in figure 20. A clear but not exact agreement with the identified magnitude is found.

Similar to the proposed on-line SDFT technique, linearization error affects the off-line identified magnitudes. An additional error in the case of the off-line Welch technique is caused by leakage. The mean cogging stiffness μ_k during identification is determined to evaluate the accuracy. Combining the measured position with the cogging torque characteristic in figure 4b leads to the time-dependent stiffness $k(t)$. The mean equals $\hat{k} = 8.70\,\mathrm{N\,mm/^\circ}$. With $\hat{k} = 5.17\,\mathrm{N\,mm/^\circ}$ being the estimated stiffness, the estimation error is found as $\varepsilon = 41\,\%$. Compared to SDFT, Welch is 10 % less accurate.

To improve the accuracy using Welch, the deflection of 6° should be limited. The only tuning option in the case of using noise injection is to change the maximum value $T_{\max}$. Further decreasing $T_{\max}$ is however not feasible because the quantization error then affects the accuracy.

The on-line SDFT technique is not only more accurate but also much more computationally efficient. This enables the parameter tracker to be implemented on the real-time motion controller. The Welch technique requires a post-processor.

The final comparison is the update time. For the benchmark, this is the measurement time of about 100 s added with some user interaction time. This user interaction time is the time needed for exporting the measured input and output signals, achieving the identified magnitudes using the Welch algorithm and applying the peak picking method. When a new parameter update is desired, the whole process needs to be repeated.

The SDFT technique delivers parameter updates each 1.25 ms without user interaction. The proposed stiffness tracker outperforms the classic Welch technique in terms of accuracy, computational efficiency and parameter update time.

5. Conclusion

Through experimental validation on a PMSM-driven rod, the proposed SDFT technique is proven to be applicable for tracking the cogging stiffness and accompanying damping. The computational efficiency of the parameter tracker is sufficiently low to be implemented as an expansion of the provided motion controller. The potential tracking errors are caused by non-linear system behaviour, quantization, noise and the use of a sliding window. For this experimental case, the maximum achievable accuracy is determined by a trade-off between the linearization and quantization error.

A benchmark with the classic off-line Welch technique shows that the proposed on-line SDFT technique is 10 % more accurate. Compared to the Welch technique, the SDFT technique is not prone to leakage and has more tuning capabilities for suppressing the linearization error.

Guidelines for suppressing the potential errors are presented and are based on initial guesses of the stiffness and damping. It is proven that a rough estimate from an impulse response enables selecting and tuning the tracking frequencies and allows convergence of the stiffness tracker. Conceptual analysis shows that convergence is guaranteed even if the initial and the actual stiffness deviate with a factor 2.

The objective is to track fast changes. Through conceptual analysis, it is found that the mean tracking error is proportional to the set fundamental frequency. The frequency selection is bounded to the low range where the stiffness affects the dynamics. The fundamental frequency thus determines the maximum rate of change of the stiffness that can accurately be tracked.

For this experimental case, the cogging stiffness changes fast within the sliding window. The proposed stiffness tracker is robust against these changes and delivers the mean value as the tracked stiffness. The capabilities of optimizing the motion control on-line based on the mean stiffness is a future research track.

A second topic for further research is limiting machine task interruption because this is not desired in the industry. Because of the early design stage of the parameter tracker, the stiffness is tracked around equilibrium to limit the linearization error. This requires interrupting the cyclic motion profiles when tracking is desired. A future research track is to investigate the tracking performance at both constant and varying speed.

References

Anuja, T. A. and M. A. N. Doss (2021). Reduction of cogging torque in surface mounted permanent magnet brushless dc motor by adapting rotor magnetic displacement. *Energies 14*.

Brandt, A. (2011). Modal analysis theory. In *Noise and Vibration Analysis*. John Wiley & Sons.

Brescia, E., D. Costantino, P. R. Massenio, V. G. Monopoli, F. Cupertino, and G. L. Cascella (2021). A design method for the cogging torque minimization of permanent magnet machines with a segmented stator core based on ann surrogate models. *Energies 14*.

Bu, F., Z. Yang, Y. Gao, Z. Pan, T. Pu, M. Degano, and C. Gerada (2021). Speed ripple reduction of direct-drive pmsm servo system at low-speed operation using virtual cogging torque control method. *IEEE Transactions on Industrial Electronics 68*, 160–174.

Dang, C., W. Wang, D. Wang, N. Tong, and X. Chen (2019). Calculation and analysis of cogging torque and end copper loss of fractional slot concentrated winding pmsm. In *2019 22nd International Conference on Electrical Machines and Systems (ICEMS)*, pp. 1–4.

Duan, X., X. Zhang, Y. Tang, and M. Hao (2021). Cogging torque reduction in pmsm in wide temperature range by response surface methodology. *Symmetry 13*.

Gavin, H. P. (2013). The levenberg-marquardt method for nonlinear least squares curve-fitting problems.

Gilardi, G., K. Szeto, S. Huard, and E. J. Park (2011). Finite element analysis of the cogging force in the linear synchronous motor array for the thirty meter telescope. *Mechatronics 21*, 116–124.

Houari, A., A. Bouabdallah, A. Djerioui, M. Machmoum, F. Auger, A. Darkawi, J.-C. Olivier, and M. F. Benkhoris (2018). An effective compensation technique for speed smoothness at low-speed operation of pmsm drives. *IEEE Transactions on Industry Applications 54*, 647–655.

Islam, R., I. Husain, A. Fardoun, and K. McLaughlin (2007). Permanent magnet synchronous motor magnet designs with skewing for torque ripple and cogging torque reduction. In *2007 IEEE Industry Applications Annual Meeting*, pp. 1552–1559.

Jacobsen, E. and R. Lyons (2003). The sliding DFT. *IEEE Signal Processing Magazine 20*, 74–80.

Jiang, W. (2023). Analysis of cogging torque of permanent magnet synchronous motor with different pole slots. *Highlights in Science, Engineering and Technology EMIS 2022*.

Keyhani, A., C. B. Studer, T. Sebastian, and S. K. Murthy (1999). Study of cogging torque in permanent magnet machines. *Electric Machines & Power Systems 27*, 665–678.

Liu, H., H. Hu, H. Chen, L. Zhang, and Y. Xing (2018). Fast and flexible selective harmonic extraction methods based on the generalized discrete fourier transform. *IEEE Transactions on Power Electronics 33*, 3484–3496.

Mengesha, S., S. Rajput, S. Lineykin, and M. Averbukh (2021). The effects of cogging torque reduction in axial flux machines. *Micromachines 12*.

Nguyen, P. H., E. Hoang, M. Gabsi, and M. Lecrivain (2010). A new method to find the fractional slot windings structures from a distributed slot windings permanent magnet synchronous machine and comparative study for a hev application. In *2010 IEEE International Conference on Industrial Technology*, pp. 317–322.

Ocak, O. and M. Aydin (2020). An innovative semi-fea based, variable magnet-step-skew to minimize cogging torque and torque pulsations in permanent magnet synchronous motors. *IEEE Access 8*, 210775–210783.

Petrov, I., P. Ponomarev, Y. Alexandrova, and J. Pyrhönen (2015). Unequal teeth widths for torque ripple reduction in permanent magnet synchronous machines with fractional-slot non-overlapping windings. *IEEE Transactions on Magnetics 51*, 1–9.

Pollefliet, J. (2017). *Power Electronics: Drive Technology and Motion Control*. Elsevier Science.

Rafii, Z. (2018). Sliding discrete fourier transform with kernel windowing [lecture notes]. *IEEE Signal Processing Magazine 35*, 88–92.

Saarakkala, S. E. and M. Hinkkanen (2015). Identification of Two-Mass Mechanical Systems Using Torque Excitation: Design and Experimental Evaluation. *IEEE Transactions on Industry Applications 51*, 4180–4189.

Shi, Z., X. Sun, Y. Cai, Z. Yang, G. Lei, Y. Guo, and J. Zhu (2019). Torque analysis and dynamic performance improvement of a pmsm for evs by skew angle optimization. *IEEE Transactions on Applied Superconductivity 29*, 1–5.

Ueda, Y., H. Takahashi, A. Ogawa, T. Akiba, and M. Yoshida (2016). Cogging-torque reduction of transverse-flux motor by skewing stator poles. *IEEE Transactions on Magnetics 52*, 1–4.

Van Oosterwyck, N., F. Vanbecelaere, M. Haemers, D. Ceulemans, K. Stockman, and S. Derammelaere (2019). CAD Enabled Trajectory Optimization and Accurate Motion Control for Repetitive Tasks. *15th IEEE International Conference on Control and Automation*.

Vanbecelaere, F., S. Derammelaere, J. Knockaert, K. Stockman, and M. Monte (2019). Identification of Dynamic Systems with Position Dependent Load Parameters. In *IEEE 7th International Conference on Control, Mechatronics and Automation*.

Vanbecelaere, F., S. Derammelaere, N. Nevaranta, J. D. Viaene, F. Verbelen, K. Stockman, and M. Monte (2020). Online Tracking of Varying Inertia using a SDFT Approach. *Mechatronics 68*.

Vanbecelaere, F., M. Monte, and K. Stockman (2023). Stiffness estimation of a lumped mass-spring system using sliding dft. In *2023 IEEE International Conference on Mechatronics (ICM)*, pp. 1–6.

Vanbecelaere, F., N. Van Oosterwyck, S. Derammelaere, A. Cuyt, M. Monte, and K. Stockman (2022). On-line motion profile optimization for reciprocating mechanisms. *Mechanism and Machine Theory 173*, 104833.

Villwock, S. and M. Pacas (2008). Application of the Welch-Method for the Identification of Two- and Three-Mass-Systems.

Wahrburg, A., E. Jelavic, S. Klose, and K. D. Listmann (2017). Robust Semi-Automatic Identification of Compliantly Coupled Two-Mass Systems. *IFAC 50*, 14569–14574.

Wang, W., H. Ma, X. Qiu, and J. Yang (2019). A calculation method for the on-load cogging torque of permanent magnet synchronous machine. *IEEE Access 7*, 106316–106326.

Wu, C.-J., M.-C. Tsai, and L.-J. Cheng (2020). Design and implementation of position-based repetitive control torque observer for cogging torque compensation in pmsm. *Applied Sciences 10*.

Yang, Y. and X. Wang (2022). Method of cogging torque reduction for built-in permanent magnet synchronous motor. *Journal of Physics: Conference Series 2246*.

Zhao, J., Y. Liu, and X. Xu (2018). Comparisons of concentrated and distributed winding pmsm in mv power generation. In *2018 XIII International Conference on Electrical Machines (ICEM)*, pp. 2437–2443.